Technische Universiteit Delft
Faculteit Elektrotechniek, Wiskunde en Informatica
Delft Institute of Applied Mathematics

Feasibility of subsurface imaging using diurnal temperature variations

Verslag ten behoeve van het
Delft Institute of Applied Mathematics
als onderdeel ter verkrijging

van de graad van

BACHELOR OF SCIENCE
in
TECHNISCHE WISKUNDE

door

Marissa Bezemer

Delft, Nederland
December 2019

BSc verslag TECHNISCHE WISKUNDE

"Feasibility of subsurface imaging using diurnal temperature variations"

Marissa Bezemer

Technische Universiteit Delft

Begeleider

Dr. N.V. Budko

Overige commissieleden

Dr. J.L.A. Dubbeldam

Drs. E.M. van Elderen

December, 2019

Delft

Contents

1 Introduction

Root and tuber crops, including cassava, yam and potatoes, are all crops that can be grown in a relatively short period of time as well as in different ecologies. Currently, the only way to monitor crop growth is to dig up the produce, after which the leftovers are disposed and thus losing the crop in the process. This current method is inefficient, time-consuming and wasteful. Other imaging techniques have thus far failed due to: a lack of open surface, physical soil properties and/or expensive equipment. Tuber breeders and farmers are therefore seeking a new method to monitor tuber growth. HZPC [1], a company dedicated to potato development and innovation, has numerous projects researching potatoes and potato growth patterns. This project will investigate a new imaging method based on observing the local changes in soil temperature and using the difference in thermal diffusivity constants of the soil and tubers. To create an imaging method, it is relevant to understand how a tuber affects the soil temperature and its surroundings as well as its magnitude. For this there are two options. The first and cheaper alternative is a pin containing equally distributed temperature sensors that can be put into the ground next to a crop. The second is a grid of temperature sensors put underneath the tubers below the surface. Both methods will be assessed for their efficacy on temperature variations as well as generating enough data to perform analyses.

To check the feasibility of these methods a model will be constructed using a temperature diffusion equation on a trench-like domain. The model will contain tubers that grow over time and have a time-varying boundary condition to account for ambient temperature changes. As tubers grow over time the interface will change as well. Thus any methods applied to the model will have to account for the moving interface. This moving interface problem can be solved using immersed finite element methods for parabolic interfaces [2]. A second method is the arbitrary Lagrangian-Eularian method [3] in which the computational mesh in the calculations may move arbitrarily to to optimize the shape of the elements. In this report both will be investigated for their usefulness. These numerical methods will then be implemented in Python using the package Feniks [4], simulated for the entirety of the tuber bulking process. The results of these simulations will then be analyzed. Based on this analysis a method will be constructed to deduce the number and size of the tubers or reconstruct an image of the tubers. The feasibility and accuracy of this method will be discussed at the end of this report. Subsurface imaging using diurnal temperature variations is not applicable to tubers if the variations caused by the tubers are not significant. If the results indicate that the temperature differences caused by the tubers are significant, this data will be used to predict the size and number of tubers or reconstruct an image of the tubers. The accuracy of this method and its availability of this method will determine its feasibility.

This research will be presented at the "10th international conference on inverse problems in engineering" (ICIPE 20) [5] in Francavilla al Mare (Chieti) Italy on May 18-20 2020.

2

Theory

In this chapter the buildup of the model will be discussed. First a heat equation will be built where any constants will be treated as functions in space and time, unlike the standard heat equation [6]. The heat equation will be further defined as well as any model variables or functions set up and named. After this two different numerical methods will be considered for the model: a Finite Element Method [2][7][8] and a Arbitrary Lagrangian Eularian Method [3].

2.1. The heat equation

In this section a heat equation will be derived where any constants are considered functions in time and space. This new heat equation will be built up from an unsteady heatflow problem similarly to the standard heat equation [6]. This unsteady heatflow problem is based on balance and conservation laws. For any region within the problem we have

$$\text{Rate of heat change within the region} + \text{Rate of heat outflow on its boundary} = \text{Rate of supply.} \tag{2.1}$$

For a time t let $f(\mathbf{x}, t)$ be the heat stored at $\mathbf{x}$, $\mathbf{q}(\mathbf{x}, t)$ be the heat flux at $\mathbf{x}$ and $S(\mathbf{x}, t)$ be the heat supply at $\mathbf{x}$. For any region Ω within the domain Equation 2.1 becomes

$$\frac{\mathrm{d}}{\mathrm{d}t}\int_{\Omega} f(\mathbf{x}, t)\,\mathrm{d}\Omega + \int_{\delta\Omega} \mathbf{q}(\mathbf{x}, t)\cdot\mathbf{n}\,\mathrm{d}\Gamma = \int_{\Omega} S(\mathbf{x}, t)\,\mathrm{d}\Omega. \tag{2.2}$$

The rules for differentiation and integration result in

$$\frac{\mathrm{d}}{\mathrm{d}t}\int_{\Omega} f(\mathbf{x}, t)\,\mathrm{d}\Omega = \int_{\Omega} \frac{\partial f(\mathbf{x}, t)}{\partial t}\,\mathrm{d}\Omega \tag{2.3}$$

and

$$\int_{\delta\Omega} \mathbf{q}(\mathbf{x}, t)\cdot\mathbf{n}\,\mathrm{d}\Gamma = \int_{\Omega} \nabla\cdot\mathbf{q}(\mathbf{x}, t)\,\mathrm{d}\Omega, \tag{2.4}$$

such that Equation 2.2 can be rewritten to

$$\int_{\Omega} \frac{\partial f(\mathbf{x}, t)}{\partial t} + \nabla\cdot\mathbf{q}(\mathbf{x}, t) - S(\mathbf{x}, t)\,\mathrm{d}\Omega = 0. \tag{2.5}$$

Since this holds for any region within the domain it follows that

$$\frac{\partial f(\mathbf{x}, t)}{\partial t} + \nabla\cdot\mathbf{q}(\mathbf{x}, t) = S(\mathbf{x}, t). \tag{2.6}$$

Heat can be measured by temperature and as such the internal heat, heat flux and heat supply can all be written as functions of the temperature $T(\mathbf{x}, t)$. The relation between the heat flux $\mathbf{q}(\mathbf{x}, t)$ and the temperature is described in Fourier's law

$$\mathbf{q}(\mathbf{x}, t) = \kappa(\mathbf{x}, t)\nabla T(\mathbf{x}, t), \tag{2.7}$$

where κ is the thermal conductivity in $\mathrm{Wm}^{-1}\mathrm{K}^{-1}$.
The internal heat $f(\mathbf{x}, t)$ can be seen as the internal energy density. The specific internal energy density of a material is a function $U = U(T)$ of the temperature and describes the heat required to raise the temperature of a unit mass to T degrees Kelvin. The internal energy density, or the internal heat, can now be given by

$$f(\mathbf{x}, t) = \rho(\mathbf{x}, t)U(T) = \rho(\mathbf{x}, t)\hat{U}(\mathbf{x}, t), \tag{2.8}$$

where ρ is the density of the material in kgm^{-3}.
Using $U(T)$ another property of the material can be derived. The specific heat $c(T)$ of a material is defined as the heat required to raise the heat of an unit mass by one degree Kelvin, therefor the definition of $U(T)$ implies that

$$c(T) = \frac{\mathrm{d}U}{\mathrm{d}T}, \tag{2.9}$$

which under constant pressure yields

$$c_p(\mathbf{x}, t) = c(T)|_p = \left.\frac{\mathrm{d}U}{\mathrm{d}T}\right|_p \tag{2.10}$$

and is constant for most materials under a wide range of temperatures.
Equation 2.7 and 2.8 can be substituted into the conversation law acquired in Equation 2.6 which leads to the following

$$\frac{\partial}{\partial t}\left(\rho(\mathbf{x}, t)\hat{U}(\mathbf{x}, t)\right) + \nabla \cdot (\kappa(\mathbf{x}, t)\nabla T(\mathbf{x}, t)) = S(\mathbf{x}, t), \tag{2.11}$$

where

$$\frac{\partial}{\partial t}(\rho\hat{U}) = \frac{\partial \rho}{\partial t}\hat{U} + \rho\frac{\mathrm{d}U}{\mathrm{d}T}\frac{\partial T}{\partial t} = \frac{\partial \rho}{\partial t}\hat{U} + \rho c_p\frac{\partial T}{\partial t}, \tag{2.12}$$

which can be approximated by

$$\frac{\partial \rho}{\partial t}\hat{U} + \rho c_p\frac{\partial T}{\partial t} \approx \rho c_p\frac{\partial T}{\partial t} \tag{2.13}$$

for small changes of density ρ relative to the changes of temperature T. By substituting Equation 2.13 back into Equation 2.11 the heat equation is found

$$c_p\rho\frac{\partial T}{\partial t} - \nabla \cdot (\kappa\nabla T) = S, \tag{2.14}$$

where the function for the heat supply S often is assumed to be known.

2.2. The model

The model will consider a section of a trench that contains growing tubers. Figure 2.1 shows a schematic respresentation of the 2D version of the model. The polygonal domain Ω is independent of the time t and consists of both soil $\Omega_s(t)$ and tubers $\Omega_t(t)$ which change over time as the tubers grow. The temperature at any point and any given time can be found using the heat equation as seen in 2.14. As the trench doesn't have its own heat-source and is instead dependent on the ambient temperature $T_A(t)$, the partial differential equation on Ω is given by

$$c_p\rho\frac{\partial T}{\partial t} - \nabla \cdot (\kappa\nabla T) = 0, \tag{2.15}$$

where the coefficients ρ, c_p and κ are different on $\Omega_s(t)$ and $\Omega_t(t)$ and therefor functions of both $\mathbf{x}$ and t. The differences will be denoted by ρ^t, c_p^t and κ^t for tubers and ρ^s, c_p^s and κ^s for soil.
In its initial state the model will contain only soil meaning $\Omega_s(0) = \Omega$ and $\Omega_t(0) = \emptyset$. The initial condition for the temperature T will be of the form

$$T(\mathbf{x}, 0) = T_0(\mathbf{x}). \tag{2.16}$$

The boundary Γ of Ω consists of boundaries Γ_a and Γ_s where the domain is neighboured by air and soil

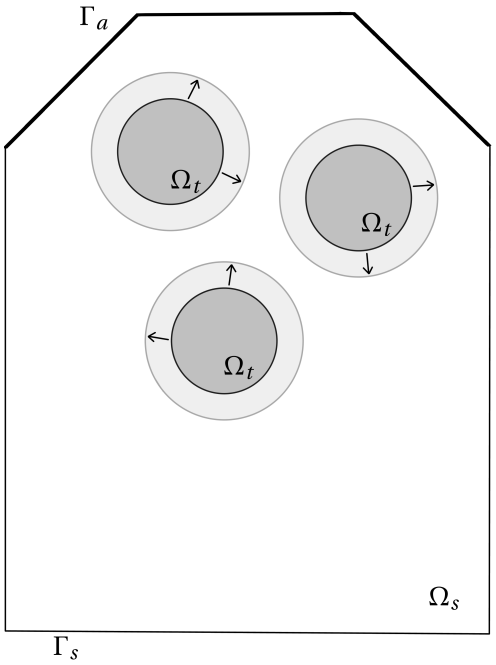

Figure 2.1: A schematic representation of the model.

respectively. The boundary Γ_a is subject to the ambient temperature $T_A(t)$. This results in the radiation of heat onto $\mathbf{x} \in \Gamma_a$ in the form of

$$\mathbf{n} \cdot (\kappa \nabla T(\mathbf{x}, t)) = \epsilon\sigma(T_A(t)^4 - T(\mathbf{x}, t)^4), \tag{2.17}$$

where ϵ is the emmisivity and σ is the Stephan-Boltsman constant [13]. The function T_A will be periodic to account for changes in temperature during the day and night. It is of the form

$$T_a(t) = c + b\sin(\frac{2\pi}{24}t), \tag{2.18}$$

when t is in hours. Here c is the average temperature and b the difference between c and the highest or lowest temperature.
Unlike Γ_a the boundary Γ_s isn't directly influenced by a function or radiation. The boundary consists of two parts, namely the bottom Γ_{s_b} of the trench and opposing boundaries Γ_{s_L} and Γ_{s_R} that split section Ω from other trenches. On Γ_{s_b} there won't be any outflow resulting in

$$\frac{\partial T}{\partial \mathbf{n}} = \nabla T \cdot \mathbf{n} = 0. \tag{2.19}$$

However at Γ_{s_L} and Γ_{s_R} the model will have to account for the influences of other trenches, which can be achieved by making these boundaries periodic. This can be written as

$$T(\mathbf{x}, t) = T(\mathbf{x}_R, t), \tag{2.20}$$

for any point $\mathbf{x} \in \Gamma_{s_R}$ and the corresponding point $\mathbf{x}_R$ on Γ_{s_L}.

2.2.1. Tubers and tuber growth

For any tuber i in the model with $i = 0, 1, \ldots, n$ we have a corresponding $\Omega_{t,i} \subset \Omega_t$. All tubers together will form Ω_t and no two tubers will overlap resulting in $\bigcup_{i=1}^{n} \Omega_{t,i} = \Omega_t$ and $\bigcap_{i=1}^{n} \Omega_{t,i} = \emptyset$ respectively. Over time the area of Ω_t will get larger as tubers grow.
Tubers in the model will be considered circles with a center point $\mathbf{c}$ and radius r. The tubers grow as the radius r increases, which will be done linearly. The growth-rate μ of r can be calculated by

$$\mu = \frac{r_{\max}}{t_{\text{period}}}, \tag{2.21}$$

where $r_{\max}$ is the maximum radius and t_{period} is the growth period of the tubers in hours. With this, the radius r of a tuber in the model equals

$$r = \mu t \tag{2.22}$$

and the area A of a tuber at time t is

$$A(t) = \pi r(t)^2 = \pi \mu^2 t^2. \tag{2.23}$$

Any tubers in the model will start growing at the same time with the same rate μ meaning that for any tubers i and j it holds that $r_i = r_j$ and $A_i = A_j$. Because of this the total area A_{total} of all tubers in the model at a time t can be calculated with

$$A_{\text{total}}(t) = \sum_{i=1}^{n} A_i(t) = n * A_1(t), \tag{2.24}$$

which is only dependent on the time t and the number n of tubers in the model.

2.3. Finite Element Method

One of the problems of the model is the moving interface. As the grid is border-confirming for the different subdomains, the grid changes with time. There has been done research towards Crank-Nicolson-type immersed finite element methods for solving equations as in our model [2]. The slow nature of tuber growth means the mesh changes will be very subtle between timesteps if Δt is picked small enough. Because of this the model will assume the mesh to be stationary at a time t. For the next step $t+1$ the results on the mesh at time t will be interpolated to the mesh of time $t+1$. When Δt is chosen small enough this shouldn't cause problems. By working under this assumption there are no other changes that have to be implemented to accommodate the changing grid and a more standard finite element method may be used. In this section a finite element method will be discussed where the equations will be discretized in time before they are written to weak formulation and discretized in space. By discretizing over time first it is possible to evaluate the functions as functions of only $\mathbf{x}$ on a stationary grid at a certain time t. The backward Euler method applied to Equation 2.15 results in:

$$c_{p,n+1}(\mathbf{x})\rho_{n+1}(\mathbf{x})\frac{T_{n+1}(\mathbf{x}) - T_n(\mathbf{x})}{\Delta t} - \nabla \cdot (\kappa_{n+1}(\mathbf{x})\nabla T_{n+1}(\mathbf{x})) = 0, \tag{2.25}$$

where $n \geq 0$ stands for the nth step of size Δt and T_0 is the initial condition of the problem. The resulting equation will be shortened to

$$\frac{c_{p,n+1}\rho_{n+1}}{\Delta t} T_{n+1} - \frac{c_{p,n+1}\rho_{n+1}}{\Delta t} T_n - \nabla \cdot (\kappa_{n+1}\nabla T_{n+1}) = 0, \tag{2.26}$$

where the dependence on $\mathbf{x}$ won't be written down explicitly.

2.3.1. Weak Formulation

To solve this problem with a Finite Element Method (FEM), it will be rewritten in weak formulation. This requires a solution space $U(\Omega)$ containing possible solutions u and test space $V(\Omega)$ containing test-functions v. The functions u will be substitute in the place of T, more precisely $T_{n+1} = u$ and $T_n = u_k$. By doing so u will stand for the function we're looking for and u_k is the solution found in a previous timestep. Note that by doing so we will need a different solution space $U(\Omega_n)$ and $V(\Omega_n)$ in

every timestep as the way they are defined here, they are defined on an Ω_n of timestep n. This method will be capable of evaluating the model at individual timesteps but will neglect the connection between timesteps. As the changes on the domain Ω will be neglectable for small enough Δt the resulting evaluation of the model at a certain timestep should still be a good approximation.

$$\frac{c_p\rho}{\Delta t}u - \frac{c_p\rho}{\Delta t}u_k - \nabla\cdot(\kappa\nabla u) = 0. \tag{2.27}$$

This will be multiplied by a test function $v \in V(\Omega)$ and integrated over Ω.

$$\int_\Omega \left[\frac{c_p\rho}{\Delta t}u - \frac{c_p\rho}{\Delta t}u_k - \nabla\cdot(\kappa\nabla u)\right] v\mathrm{d}\Omega = 0, \tag{2.28}$$

which can be written as

$$\int_\Omega \frac{c_p\rho}{\Delta t}(u-u_k)v\mathrm{d}\Omega - \int_\Omega \nabla\cdot(\kappa\nabla u)v\mathrm{d}\Omega = 0. \tag{2.29}$$

Since we have that

$$\nabla\cdot(v\kappa\nabla u) = (\nabla v)\cdot(\kappa\nabla u) + v\nabla\cdot(\kappa\nabla u) \tag{2.30}$$

we can write

$$\int_\Omega \nabla\cdot(\kappa\nabla u)v\mathrm{d}\Omega = -\int_\Omega (\nabla v)\cdot(\kappa\nabla u)\mathrm{d}\Omega + \int_\Omega \nabla\cdot(v\kappa\nabla u)\mathrm{d}\Omega \tag{2.31}$$

$$= -\int_\Omega (\nabla v)\cdot(\kappa\nabla u)\mathrm{d}\Omega + \int_\Gamma \kappa(\nabla u\cdot\mathbf{n})v\mathrm{d}\Gamma \tag{2.32}$$

and substitute this back into Equation 2.29. The result yields

$$\int_\Omega \frac{c_p\rho}{\Delta t}(u-u_k)v\mathrm{d}\Omega + \int_\Omega (\nabla v)\cdot(\kappa\nabla u)\mathrm{d}\Omega - \int_\Gamma \kappa(\nabla u\cdot\mathbf{n})v\mathrm{d}\Gamma = 0, \tag{2.33}$$

which also contains an integral over the boundary $\Gamma = \Gamma_a \cup \Gamma_s$. When this integral is split over the different parts of the boundaries, the boundary conditions for each boundary can be applied. Now using Equations 2.19, 2.20 and 2.17

$$\int_{\Gamma_a} \kappa(\nabla u\cdot\mathbf{n})v\mathrm{d}\Gamma = \epsilon\sigma\int_{\Gamma_a}(T_a^4 - u^4)v\mathrm{d}\Gamma, \tag{2.34}$$

$$\int_{\Gamma_{s_b}} \kappa(\nabla u\cdot\mathbf{n})v\mathrm{d}\Gamma = 0, \tag{2.35}$$

$$\int_{\Gamma_{s_r}} \kappa(\nabla u\cdot\mathbf{n})v\mathrm{d}\Gamma = \int_{\Gamma_{s_l}} \kappa(\nabla u\cdot\mathbf{n})v\mathrm{d}\Gamma. \tag{2.36}$$

To accommodate the periodic boundary the periodicity on the boundaries will be added as a property of the function space and the test function space will be adjusted accordingly.
For $u \in U(\Omega) = \{f \mid f(\Gamma_{s_R}) = f(\Gamma_{s_L})\}$ and $v \in V(\Omega) = \{g \mid g(\Gamma_{s_R}) = g(\Gamma_{s_L})\}$ the weak formulation of the partial differential equation becomes

$$0 = \int_\Omega \frac{c_p\rho}{\Delta t}(u-u_k)v\mathrm{d}\Omega + \int_\Omega (\nabla v)\cdot(\kappa\nabla u)\mathrm{d}\Omega - \epsilon\sigma\int_{\Gamma_a}(T_a^4 - u^4)v\mathrm{d}\Gamma, \tag{2.37}$$

which can be rewritten to

$$0 = \int_\Omega (u-u_k)v\mathrm{d}\Omega + \int_\Omega (\nabla v)\cdot(D\nabla u)\mathrm{d}\Omega - \epsilon\sigma\int_{\Gamma_a}\frac{\Delta t}{c_p\rho}(T_a^4 - u^4)v\mathrm{d}\Gamma, \tag{2.38}$$

with $D = \frac{\kappa\Delta t}{c_p\rho}$. The constants in the border integral will always be assumed to be those of soil, as tubers grow underground and are therefore denoted by c_p^s and ρ^s respectively. In the case without tubers all constants would be soil-only and D will be denoted D_s.

In order to solve it numerically the dicretization in $\mathbf{x}$ has to be completed. To do this a basis for V has to be chosen. Let $\phi_{k,i}$ be Lagrangian basis functions on Ω for $i = 1, \ldots, m$, then

$$U(\Omega) = \{u_k = \sum_{i=1}^{m} a_{i,k}\psi_{i,k}(\mathbf{x})\} \tag{2.39}$$

$$V(\Omega) = \{v_k = \psi_{i,k}(\mathbf{x})\}. \tag{2.40}$$

Substitution of the functions into Equation 2.37 will result in a system that can be discretized in $\mathbf{x}$ and rewritten to a system that can be assembled into matrices.

2.4. Arbitrary Lagrangian Eulerian method

Another option is to apply the finite element method using the arbitrary Lagrangian-Eularian description [3]. This method will result in an extra term to compensate for the changing grid. As tubers grow the mesh will change, the movement of a node $\mathbf{x} = (x, y)$ can be described by the known function $\overrightarrow{r}(t) = (\tilde{x}(t), \tilde{y}(y))$. Substituting $T(x, y, t) = \tilde{T}(\tilde{x}(t), \tilde{y}(t), t)$ will result in

$$\frac{\partial \tilde{T}}{\partial t} = \frac{\partial \tilde{T}}{\partial t} + \tilde{\nabla}\tilde{T} \cdot \frac{\mathrm{d}\overrightarrow{r}}{\mathrm{d}t}, \tag{2.41}$$

for $\tilde{\nabla} = \frac{\partial}{\partial \tilde{x}} + \frac{\partial}{\partial \tilde{y}}$ meaning the partial differential equation becomes

$$\tilde{c_p}\tilde{\rho}(\frac{\partial \tilde{T}}{\partial t} + \tilde{\nabla}\tilde{T} \cdot \frac{\mathrm{d}\overrightarrow{r}}{\mathrm{d}t}) - \tilde{\nabla} \cdot (\tilde{\kappa}\tilde{\nabla}\tilde{T}) = 0 \tag{2.42}$$

where $\tilde{c}_p$, $\tilde{\rho}$ and $\tilde{\kappa}$ are functions of $\overrightarrow{r}(t)$ and t.
This partial differential equation can be discretized over time using the backward Euler method. Note that since $\overrightarrow{r}(t)$ is a known function we can calculate $\frac{\partial \overrightarrow{r}}{\partial t}(t) = R(t)$ for any given t, resulting in

$$\frac{\tilde{c}_{p,n+1}\tilde{\rho}_{n+1}}{\Delta t}\tilde{T}_{n+1} - \frac{\tilde{c}_{p,n+1}\tilde{\rho}_{n+1}}{\Delta t}\tilde{T}_n + \tilde{\nabla}\tilde{T}_{n+1} \cdot R_{n+1} - \nabla \cdot (\tilde{\kappa}_{n+1}\nabla\tilde{T}_{n+1}) = 0, \tag{2.43}$$

where $n \geq 0$ stands for the nth step of size Δt, $\tilde{T}_0$ is the initial condition of the problem and the dependence to $(\tilde{x}(t), \tilde{y}(t))$ isn't written down explicitly.
Let $U(\Omega)$ be a solution space with $U(\Omega) = \{\tilde{u} \mid \tilde{u}(\Gamma_{s_R} = \tilde{u}(\Gamma_{s_L})\}$ and $V(\Omega)$ be a test function space with $V(\Omega) = \{\tilde{v} \mid \tilde{v}(\Gamma_{s_R} = \tilde{v}(\Gamma_{s_L})\}$ for a certain type of functions $\tilde{u}$ and $\tilde{v}$ respectively. The functions $\tilde{u} \in U(\Omega)$ will be substituted in the place of $\tilde{T}$ as follows $\tilde{T}_n = \tilde{u}_k$ and $\tilde{T}_{n+1} = \tilde{u}$, meaning $\tilde{u}$ will stand for the solution we will be looking for and $\tilde{u}_k$ the solution for the previous time-step. Similarly $\tilde{c}_{p,n+1}, \tilde{\rho}_{n+1}$ and $\tilde{\kappa}_{n+1}$ become $\tilde{c}_p, \tilde{\rho}$ and $\tilde{\kappa}$ respectively. Since $\mathbf{x}$ is now a function of t, unlike previously, the function space does not have to be adjusted at every time step. The weak formulation for the partial differential equation is found by the same derivation as before with one extra term. Now for $\tilde{u} \in U(\Omega)$ and $\tilde{v} \in V(\Omega)$ the weak formulation becomes

$$0 = \int_\Omega \frac{\tilde{c}_p\tilde{\rho}}{\Delta t}(\tilde{u} - \tilde{u}_k)\tilde{v}\mathrm{d}\Omega + \int_\Omega (\nabla\tilde{v}) \cdot (\tilde{\kappa}\nabla\tilde{u})\mathrm{d}\Omega + \int_\Omega \tilde{c}_p\tilde{\rho}\tilde{\nabla}\tilde{u} \cdot \frac{\partial \overrightarrow{r}}{\partial t}\tilde{v}\mathrm{d}\Omega - \epsilon\sigma\int_{\Gamma_a}(T_a^4 - \tilde{u}^4)\tilde{v}\mathrm{d}\Gamma. \tag{2.44}$$

In comparison to Equation 2.37 the biggest difference lies in the extra term

$$\int_\Omega \tilde{c}_p\tilde{\rho}\tilde{\nabla}\tilde{u} \cdot \frac{\partial \overrightarrow{r}}{\partial t}\tilde{v}\mathrm{d}\Omega. \tag{2.45}$$

The function $\frac{\partial \overrightarrow{r}}{\partial t}$ is the derivative of the function $\overrightarrow{r}$ that describes how the mesh moves when tubers grow. The growth rate of a tuber per t is of order 10^{-5} and $\frac{\partial \overrightarrow{r}}{\partial t}$ will be of similar order. It is relatively smaller than the other functions and therefor the effects of the integral will be neglectable in comparison to the other terms.

3

Simulations

In this chapter the model will be simulated. The simulations will be on a polygonal domain, which will have a border-confirming and non-uniform mesh. A new grid will be generated for each step in time, solutions on the old grid are interpolated to the new grid to account for any changes between steps. An example of the generated meshes at different days can be seen in Figure 3.1. Along three different lines the temperature data of the simulations will be stored, along the horizontal line beneath the tubers, the line to the left and the line to the right which are L_b, L_l and L_r respectively and contain a set of uniformly distributed nodes along the line.

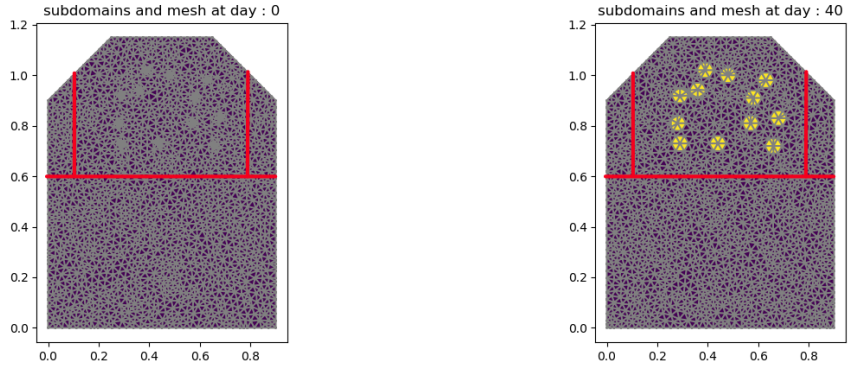

Figure 3.1: A figure depicting the mesh and domains at different stages with the three measuring lines

The temperature data stored will be known as T_D and is a discrete function of t and $\mathbf{x} \in L$. All constants used in the simulations are as seen in table 3.1 [9] [10] [11] [12] [13].

Variable	Value	Units	Variable	Value	Units
κ^s	0,3	$W/(m \cdot K)$	σ	$5,670374 \cdot 10^{-8}$	Wm^2/K^4
κ^t	0,56	$W/(m \cdot K)$	ϵ	0,8	
ρ^s	1300	kg/m^3	Δt	3600	s
ρ^t	1079	kg/m^3	T_{period}	$6,048 \cdot 10^6$	s
c_p^s	800	$J/(kg \cdot K)$	c	288	K
c_p^t	4036	$J/(kg \cdot K)$	b	5	K
D_s	$2,88 \cdot 10^{-7}$	Wm^2/J	$r_{\max}$	0,06	m
D_t	$1,29 \cdot 10^{-7}$	Wm^2/J	μ	$9,92 \cdot 10^{-6}$	m/s

Table 3.1: Table containing all constants used for simulation

Tubers within the model are restrained to fall within a certain region of the trench. They're restricted to be $0,1$ meter underground and the domain surrounded by L_r, L_l and L_b. Figures shown of simulated data will use a model containing 12 growing tubers unless specified otherwise.

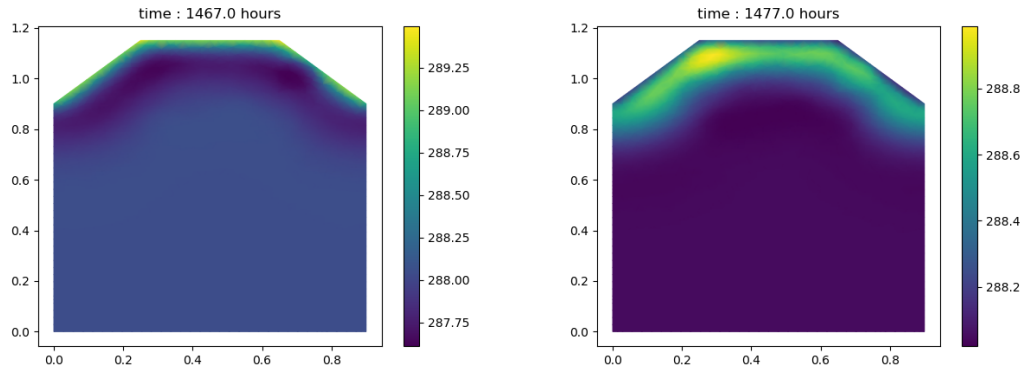

Figure 3.2: A figure depicting the simulated temperature on the entire domain at two different times during the day.

Simulations made obtain the temperatures at nodes through the grid. As seen in Figure 3.2 the temperature appears to primarily move vertically through the domain, which should mean tubers will cause a different on L_b. The simulated temperatures will only be stored along the three different measuring lines. The temperature data T_D is stored per day k and for all nodes $\mathbf{x} \in L_i$ where $i \in \{r, l, b\}$. When referring to stored data from simulations T_D may be written as T_D^k to refer to the data on a single day.

3.1. Effects of soil and tubers on the temperature

In this section the results and findings of the simulations will be discussed. When looking at the temperature changes underground over the span of a day the periodicity of the ambient temperature is still visible. The sine of the ambient temperature has dampened and shifted based on the depth and the total size of the tubers.
Figure 3.3 shows these effects. The deeper into the soil, the lower the amplitude of the temperature becomes and the larger the phase shift will be. When tubers are added the same effects are visible again as the amplitude gets dampened more and the phase shifts more again.

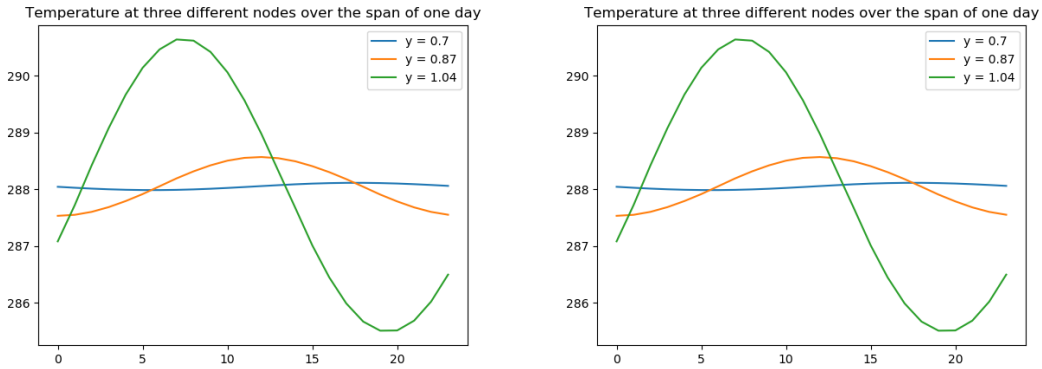

Figure 3.3: Left: the temperature (vertically) against the time (horizontally) in nodes at a different height in the model. Right: the temperature (vertically) against the time (horizontally) in the same node at different days under a bush of growing tubers

A more detailed view on both the effects of depth and tubers can be found in Figure 3.4. As the model has a polygonal shape, when looking at temperature data along [NAME], the nodes to the left and right

will be less deep underground than nodes in the middle. This means that along L_b we will see a decrease or increase in the amplitude and location of the minimum based off of depth only.

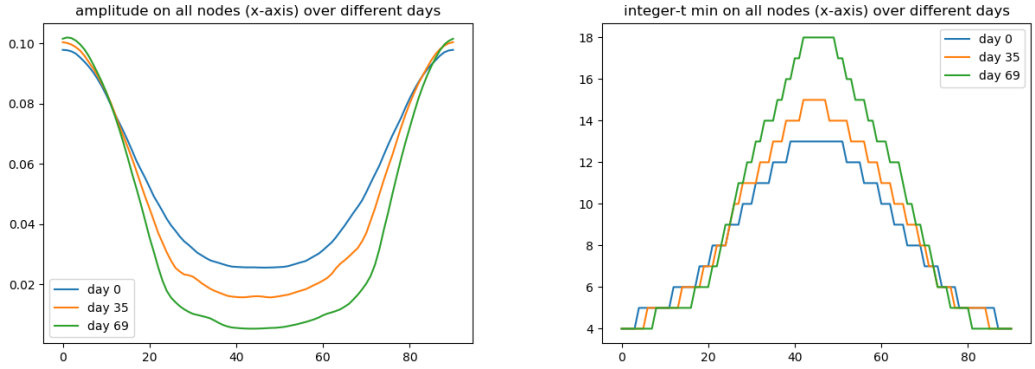

Figure 3.4: Left: the amplitude in temperature on a certain day for each the nodes on the horizontal measure line. Right: the t in hours at which the minimum temperature is reached on a certain day for each of the nodes on the horizontal measure line.

In Figure 3.4 the amplitudes and phase shift in hours for the temperature data on days 0, 35 and 69 are shown for each node on L_b. As a result it is visible how the size of tubers affects the amplitude and location of the minimum more clearly. The amplitude on the edges appear unaffected by the tubers, most likely due to the tubers being more focused to the center of the trench. as seen in Figure 3.1. The temperature in the nodes in the middle of L_b do show the effects of tuber growth. The amplitude gets lower, and so the sine more dampened, the larger tubers grow and at its smallest a precision of 10^{-3} might be needed to be able to measure temperature differences under the ground. The location of the minimum also changes. At day 0 there are no tubers and the location of the minimum only shows the shift based on the depth. As the nodes get deeper underground the hour at which the minimum is found gets delayed: the phase shift. This effect is strengthened on later days where tubers have grown and are affecting the time before the minimum on that day is reached.

4

Effective inversion

In this chapter a different method for determining the amount of tubers will be explored. The data itself is unclear as to determine size or locations of tubers. As a result, another method is needed to estimate the quantity of tubers underground - or at the least be able to monitor growth more effectively. Effective inversion has been implemented to approximate in-homogeneous models for electromagnetic waves [14][15] [16] and although it will not result in the exact size or location of tubers it might be able to give an approximation of the relation between soil and tubers. It is important to note that problems like this often are ill posed due to the existence of multiple solutions. The goal for this chapter therefor is not to directly determine the number of tubers, their size or their locations, but to approximate the in-homogeneous model presented as well as possible and gain information on tuber growth from this approximation. The focus lays on the approximation of the in-homogeneous model and the information that can be extracted from the approximation.
In effective inversion the data of the in-homogeneous model will be fitted to results of an homogeneous model that varies the constants used. The constants ρ, κ and c_p can be reduced to only the constant D as seen before. The homogeneous model will be called $T_M(D)$ and is dependent on D.
The model $T_M(D)$ will be a lot less complex than T_D, it consists of two homogeneous subdomains. The constant D within the model as seen in Equation 2.38 will be a function of $\mathbf{x}$. Only in the domain where tubers are allowed to grow the constant D as given in $T_M(D)$ will be applied, the rest of the domain uses soil constants D_s, c_p^s, ρ^s. This will allow $T_M(D)$ to be better fitted to T_D. Simulations of this model will be made on a less fine grid as simulations have to run faster. Other than the grid it's simulated under the same circumstances as T_D. To fit the data of $T_M(D)$ to T_D a functional $F[D]$ is needed that will minimize the difference between $T_M(D)$ and T_D with respect to D.
The D for which $F[D]$ is minimal will be called D_{eff} and will be considered an indicator of the amount of tubers. When $D_{\text{eff}} = D_s$ it's an indication there are no tubers while $D_{\text{eff}} \to D_t$ indicates there are tubers. Because of this the following assumption for D_{eff} holds

$$D_t \leq D_{\text{eff}} \leq D_s, \tag{4.1}$$

since $D_t \leq D_s$. Hypothetically D_{eff} has a similar dependence on the volume fraction of Ω and Ω_t as seen in the Maxwell-Garnett [14] equation, which in this situation could result in

$$D_{\text{eff}}(t) = \frac{V(\Omega_t(t))}{V(\Omega)} D_t + \frac{V(\Omega) - V(\Omega_t(t))}{V(\Omega)} D_s, \tag{4.2}$$

at a certain time t, where the function $V(\Omega)$ stands for the area of the domain, so $V(\Omega_t(t)) = A_{\text{total}}(t)$.
To reach find the empherical D_{eff} different functionals will be tried and tested. After which better ways to minimize and determine the D_{eff} based on the functional will be discussed.

4.1. Cost functionals

A cost functional $F[D]$ can be determined for any set of $t \in T_{\text{period}}$ and any collection of nodes $\mathbf{x} \in \Omega$. All cost functionals will be determined for the $T_M^k(D)$ and ${}^kT_D$ on a certain day k and along all nodes $\mathbf{x} \in L_b$, where T^k will often simply be denoted T. Basing the cost functional on a complete period of the temperature will account of all changes and differences found during the day as well as the differences between nodes along L_b. A cost functional must have the following properties:

$$F[D] = 0 \Longleftrightarrow T_M(D) = T_D \tag{4.3}$$

and

$$F[D] \geq 0 \Longleftrightarrow T_M(D) \neq T_D, \tag{4.4}$$

and will have a minimum at D for which $T_M(D)$ fits T_D best.

4.1.1. SSD functional

A logical start would be by looking at least squares fitting. The resulting functional would be defined as the following sum of squared differences (SSD):

$$F[D] = \sum_{j=1}^{24} \sum_{i=1}^{n} |T_M(D, x_i, t_j) - T_D(x_i, t_j)|^2, \tag{4.5}$$

for which it is clear that the properties 4.3 and 4.4 hold. It can be normalized by

$$F_{\text{norm}}[D] = \frac{\sum_{j=1}^{24} \sum_{i=1}^{n} |T_M(D, x_i, t_j) - T_D(x_i, t_j)|^2}{\sum_{j=1}^{24} \sum_{i=1}^{n} |T_D(x_i, t_j)|^2}, \tag{4.6}$$

however F_{norm} doesn't give the expected results.
Figure 4.1 shows $F[D]$ and F_{norm} with respect to different $D \in [D_t, D_s]$ on two days within the growing period. The curves do follow expectations within the interval $[D_t, D_s]$. At the start of the growth season, without tubers, the minimum of $F[D]$ is found at D_s while the minimum moves towards D_t on later days. Although the curves for $F[D]$ and $F_{\text{norm}}[D]$ are similar, $F_{\text{norm}}[D]$ is not properly normalized. The values for $F_{\text{norm}}[D]$ are extremely low indicating an error in the normalization.
To investigate this a closer look at $F[D]$ and $F_{\text{norm}}[D]$ are needed. A simplified version of $T(x,t)$ would be a sine with certain phase shift and amplitude. As tubers don't significantly grow within the span of a day the phase shift and amplitude are only dependent on x and not on t. Define

$$T_D(x,t) = c + d(x)\sin(\frac{2\pi}{24}t + \phi(x)) \tag{4.7}$$

$$T_M(D,x,t) = c + m(D,x)\sin(\frac{2\pi}{24}t + \psi(D,x)), \tag{4.8}$$

where d and m are the amplitudes, ϕ and ψ are the phase shifts and c the average temperature. The functions are real and continuous in t.
Substituting these functions in $F_{\text{norm}}[D]$ results in

$$F_{\text{norm}}[D] = \frac{\sum_{j=1}^{24} \sum_{i=1}^{n} (m_i(D)\sin(\frac{2\pi}{24}t_j + \psi_i(D)) - d_i\sin(\frac{2\pi}{24}t_j + \phi_i))^2}{\sum_{j=1}^{24} \sum_{i=1}^{n} (c + d_i\sin(\frac{2\pi}{24}t_j + \phi_i))^2}, \tag{4.9}$$

where $m_i(D) = m(D, x_i)$ and $d_i = d(x_i)$. Here the absolute value doesn't have to be taken, as the square of real functions is always positive. Due to the continuity in t and

$$\sum_{j=1}^{24} \sum_{i=1}^{n} (f(x_i,t))^2 = \sum_{i=1}^{n} \sum_{j=1}^{24} (f(x_i,t))^2 = \sum_{i=1}^{n} \int_1^{24} (f(x_i,t))^2 dt,$$

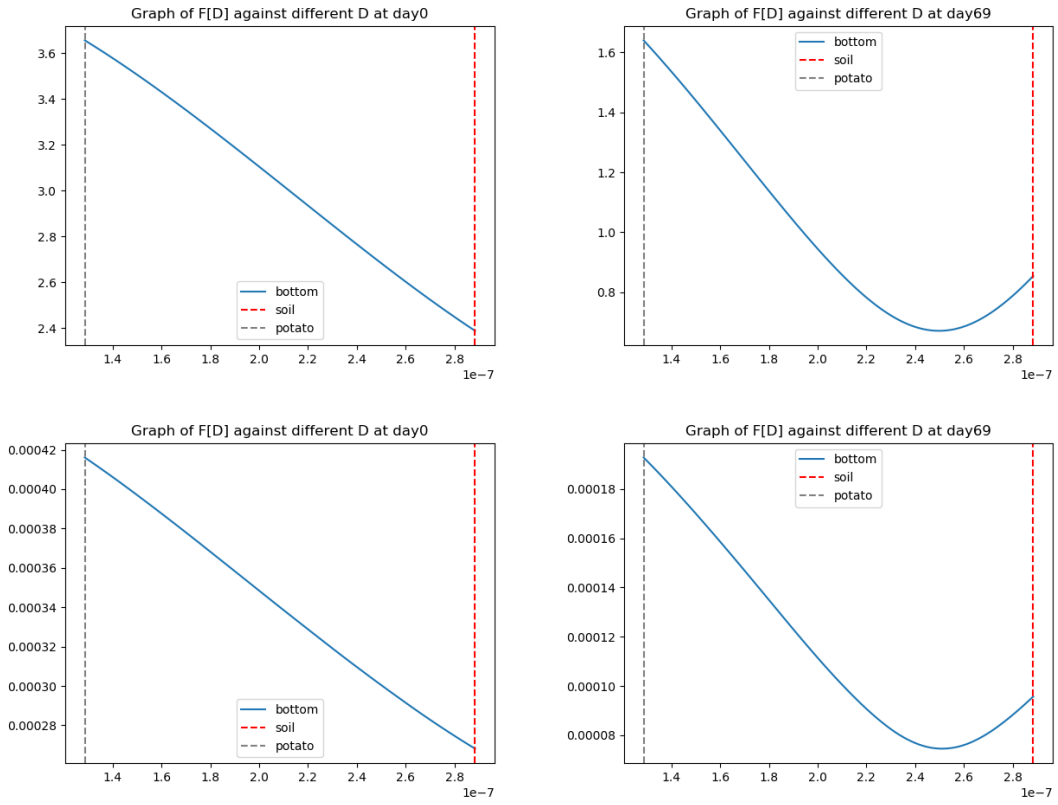

Figure 4.1: Top: Graph of $F[D]$ against D on the first day (left) and last day (right). Bottom: Graph of $F_{\text{norm}}[D]$ against D on the first day (left) and last day (right).

$F_{\text{norm}}[D]$ can be rewritten to

$$F_{\text{norm}}[D] = \frac{\sum_{i=1}^{n} \int_{j=1}^{24} (m_i(D)\sin(\frac{2\pi}{24}t_j + \psi_i(D)) - d_i \sin(\frac{2\pi}{24}t_j + \phi_i))^2}{\sum_{i=1}^{n} \int_{j=1}^{24} (c + d_i \sin(\frac{2\pi}{24}t_j + \phi_i))^2},$$

which is equal to

$$F_{\text{norm}}[D] = \frac{\pi \sum_{i=1}^{n} (d_i^2 + m_i^2(D) - 2d_i m_i(D) cos(\psi_i(D) - \phi_i))}{\pi \sum_{i=1}^{n} (2c^2 + d_i^2)}. \tag{4.10}$$

The result shows properties 4.3 and 4.4 still apply as well as the reason behind the extremely low values of $F_{\text{norm}}[D]$. The denominator is a lot larger than the numerator due to the c^2 in the denominator.
As a result a better way to normalize $F[D]$ is

$$F_{\text{norm}}[D] = \frac{\sum_{j=1}^{24} \sum_{i=1}^{n} |T_M(D, x_i, t_j) - T_D(x_i, t_j)|^2}{\sum_{j=1}^{24} \sum_{i=1}^{n} |T_D(x_i, t_j) - \overline{T}_D(x_i)|^2}, \tag{4.11}$$

where

$$\overline{T}_D(x_i) = \sum_{j=1}^{24} T_D(x_i, t_j), \tag{4.12}$$

which will be equal to c if T_D is as proposed in 4.7 resolving the previous issue. The results do confirm this theory as can be observed in Figure 4.2.
Here, as expected, the curve still closely resembles that of $F[D]$ however the values of F_{norm} are lower

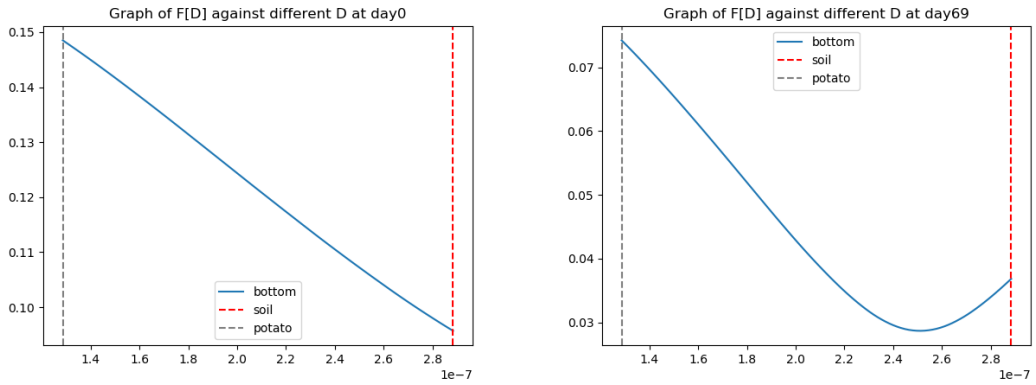

Figure 4.2: Figure depicting the corrected $F_{\text{norm}}[D]$ against D on the first day (left) and last day (right).

without being extremely low. However it is important to note that this functional isn't without error. The functional can give a false minimum. $F_{\text{norm}}[D]$ written similarly to equation 4.10 results in

$$F_{\text{norm}}[D] = \frac{\sum_{i=1}^{n}(d_i^2 + m_i^2(D) - 2d_i m_i(D)cos(\psi_i(D) - \phi_i))}{\sum_{i=1}^{n} d_i^2}, \tag{4.13}$$

which when looking at only one node $\mathbf{x}_i$ means

$$F_{\text{norm}}[D](\mathbf{x}_i) = 1 + (\frac{m_i(D)}{d_i})^2 - 2\frac{m_i(D)}{d_i}cos(\psi_i(D) - \phi_i) \tag{4.14}$$

and is

$$F_{\text{norm}}[D](\mathbf{x}_i) = \begin{cases} (1 - \frac{m_i(D)}{d_i})^2 & ,\psi_i(D) = \phi_i + 2k\pi \\ (1 + \frac{m_i(D)}{d_i})^2 & ,\psi_i(D) - \phi_i = \pi + 2k\pi \\ 1 + (\frac{m_i(D)}{d_i})^2 & ,\psi_i(D) - \phi_i = \frac{1}{2}\pi + k\pi \end{cases} \tag{4.15}$$

for $k \in Z$. Due to the behaviour of the cosine the difference in phase can cause a minimum to occur periodically with respect to D or even cause a possibly false large value for certain phase shifts.
Figure 4.3 shows for which D the lowest value of $F[D]$ is reached for each day of T_{period}. The figure shows that the D corresponding to the smallest value of $F_{\text{norm}}[D]$ decreases over time, which is what was expected since $D_t < D_s$. Even so, the flat slope is an indicator the SSD functional might not be sensitive enough to the tubers. Due to this other cost functionals need to be explored.

4.1.2. Correlation-based functional

A better way to compare periodic functions might be to look at their correlation $C(T, \mathbf{x}_i)$ with

$$C(T, x_i) = \frac{\sum_{j=1}^{24}(T(x_i, t_j) - \overline{T}(x_i, t_j)(T_a(x_i, t_j) - \overline{T}_a(x_i, t_j))}{\sigma(T(x_i))\sigma(T_a(x_i))} \tag{4.16}$$

where T_a is a homogeneous model with only soil, $\overline{T}$ is as defined in equation 4.12 and

$$\sigma(T(x_i)) = \sqrt{\sum_{j=1}^{24} |T(x_i, t_j) - \overline{T}(x_i)|^2}. \tag{4.17}$$

The correlation between $T_D(x, t)$ as defined in equation 4.7 and

$$T_a(x, t) = c + a(x)\sin(\frac{2\pi}{24}t + \rho(x)) \tag{4.18}$$

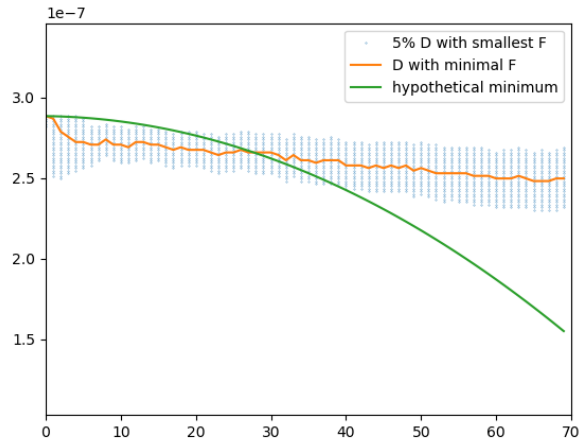

Figure 4.3: Graph depicting the D for which the functional 4.11 smallest against the days of T_{period}. As comparison the D_{eff} as in equation 4.2 and the D corresponding to the 5% smallest F[D] are drawn.

is

$$C(T_D(x_i), x_i) = \cos(\rho_i - \phi_i), \tag{4.19}$$

where $\rho(x_i) = \rho_i$ and $\phi(x_i) = \phi_i$ and therefor correlations are solely dependent on phase shifts. The correlation between two models gives the following results depending on the phase shifts

$$C(T_D(x_i), x_i) = \begin{cases} 1 & , \rho_i = \phi_i + 2k\pi, \\ 0 & , \rho_i - \phi_i = \frac{1}{2}\pi + k\pi, \\ -1 & , \rho_i - \phi_i = \pi + 2k\pi \end{cases} \tag{4.20}$$

with $k \in \mathrm{Z}$. A functional based off of correlation would as a result also be only dependent on phase shifts, rather than a combination of phase shifts and amplitude. The proposed correlation-based functional would be

$$F[D] = \frac{\sum_{i=1}^{n} |C(T_D(x_i), x_i) - C(T_M(D, x_i), x_i)|^2}{\sum_{i=1}^{n} |C(T_D(x_i), x_i)|^2} \tag{4.21}$$

for which the properties 4.3 and 4.4 do appear to hold. There are some issues with using the correlations in this manner due to the way the correlations are defined, which are also visible when looking at Figure 4.4 showing the behaviour of the functional for different D for a certain day.
When T_D closely resembles T_a the functional may give an incorrect minimum and the shifting phases mean multiple minima, or a flattened minimum may occur. This can make it hard to locate a correct minimum, as demonstrated in Figure 4.5.
The absolute minimum of $F[D]$ with respect to D will move to the right, then jump to moving to the left again. It is caused by the flattened tail consisting of two minima, as seen in Figure 4.4, of which only one is found. The range of D for which $F[D]$ close to the absolute minimum is found is also evidence of this tail. The band gets broader even after the sudden drop, to the point it gets split into two smaller bands. After the drop the absolute minimum behaves as expected and follows a similar path as the minimum of the SSD functional, be it with a steeper slope. Improvements on finding a minimum are needed. The figure, together with Figure 4.3, is enough to say D_{eff} does not behave like the hypothesis. The hypothesis is a quadratic function of r while the empirical D_{eff} are appearing to be linear. It may be concluded that equation 4.2 does not hold.

4.2. Behaviour of the minimum

As taking the absolute minimum has its issues a different algorithm to select a minimum has to be implemented. From earlier results we've seen that the expected minimum is to the left of the absolute

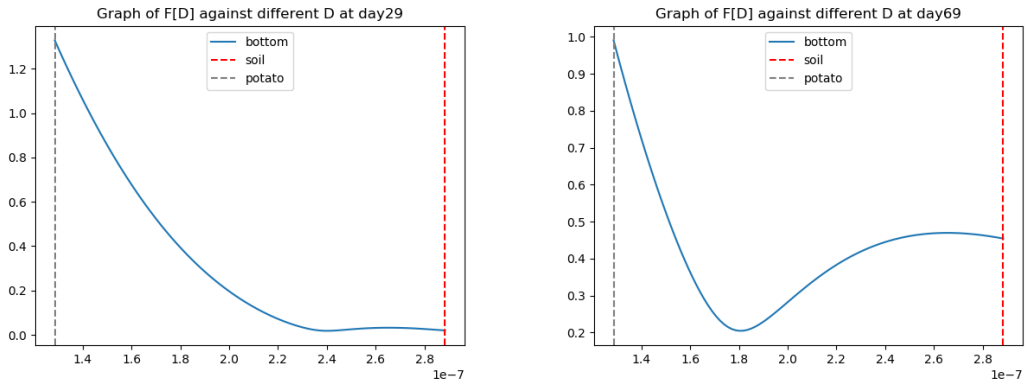

Figure 4.4: Left: the amplitude in temperature on a certain day for each the nodes on the horizontal measure line. Right: the t in hours at which the minimum temperature is reached on a certain day for each of the nodes on the horizontal measure line.

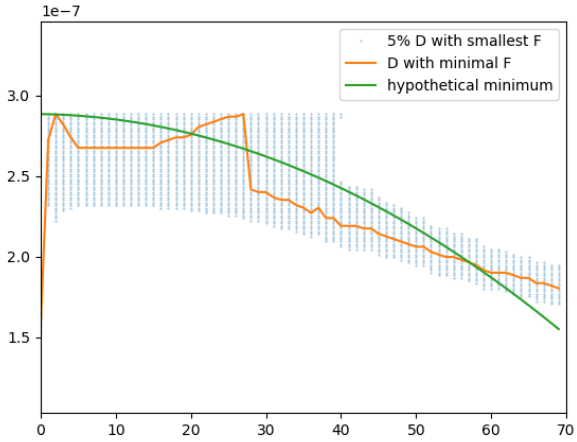

Figure 4.5: Graph depicting the D for which the correlation-based function is smallest against the days of T_{period}. As comparison the D_{eff} as in equation 4.2 and the D corresponding to the 5% smallest F[D] are drawn.

minimum, meaning the absolute minimum has a higher value for D than the expected minimum. In this model tubers strictly grow and as they grow $D \to D_t$ the following holds for minima D_i, D_j on days i, j

$$D_j \leq D_i \iff i \leq j. \tag{4.22}$$

A different algorithm can be implemented using these assumptions where on a day k we have

$$D^k_{\text{min}} \begin{cases} \arg\min F^k[D] & , D \in [D_t, D^{k-1}_{\text{min}}] \\ D^{k-1}_{\text{min}} & , \text{otherwise} \end{cases} \tag{4.23}$$

where $D^0_{\text{min}} = D_s$. The result, compared to the previously found absolute minima, is visible in Figure 4.6. The peeks are now corrected by drawing them horizontally until a day k where the $\arg\min F^k[D]$ has $D \in [D_t, D^{k-1}_{\text{min}}]$, the rest of the curve remains the same.
Instead of still trying to find $\arg\min F^k[D]$ for all D it's also possible to set

$$D^k_{\text{min}} = \arg \min_{D \in [D_t, D^{k-1}_{\text{min}}]} F[D], \tag{4.24}$$

where D^k_{min} will at most be equal to D^{k-1}_{min}. Although both algorithms appear to be similar, 4.24 is able to refine the curve by finding the second minimum as absolute minimum now the search area for D has

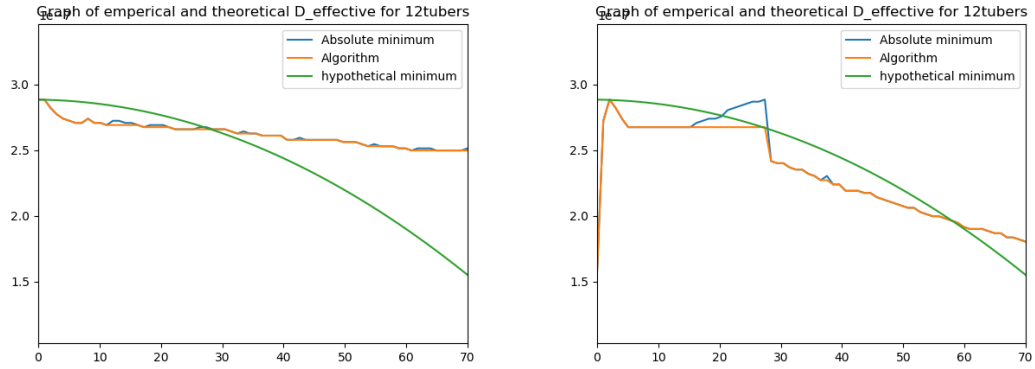

Figure 4.6: Left: the absolute and corrected minimum using 4.23 for the SSD functional. Right: the absolute and corrected minimum using 4.23 for the correlation-based functional.

been decreased. This is illustrated in figure 4.7. The SSD functional is least affected by these changes as it already was mostly strictly decreasing, however the curve of the correlation-based functional seems affected positively. The second minimum is the absolute minimum for a part of the peek and can now be find by limiting the search area for D. Both curves appear to be linear. Under the assumption that the curves are linear, a line can be fitted and extrapolated to correct for the errors in the early weeks of the correlation-based functional. The line should be based on the lower end of the curve, from the moment the horizontal area starts decreasing again, and the point $(t, D) = (0.0, D_s)$. Examples are seen in Figure 4.8.

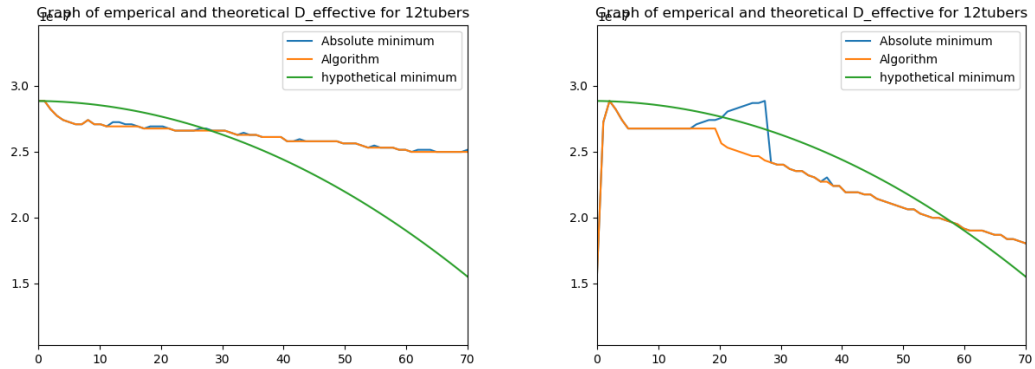

Figure 4.7: Left: the absolute and corrected minimum using 4.24 for the SSD functional. Right: the absolute and corrected minimum using 4.24 for the correlation-based functional.

In Figure 4.8 it's seen how a straight-line fits $D_{\min}$ for the correlation-based functional. The extrapolated data starts and ends as expected while following the empirical curve closely. The two models each have different numbers of tubers growing, which has effect on the slope (and endpoint) of the curve.

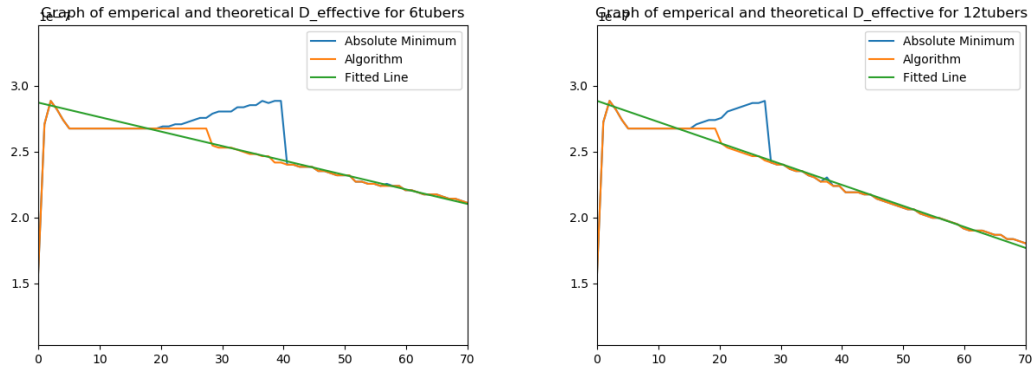

Figure 4.8: The absolute minimum, corrected minimum and a fitted line based on the lower end of the curve for 6 tubers (left) and 12 tubers (right) of the correlation-based functional.

5

Feasibility

In this chapter the feasibility of subsurface imaging using diurnal temperature variations will be discussed based on the previously shown results. Based on these results the applicability of subsurface imaging will be decided.
In chapter 3 has been shown that it is possible to detect differences between stages with and without tubers using the model. For a periodic temperature change these differences are primarily visible as phase-shifts and amplitude changes. These differences can be used to monitor growth. However, these are not specific enough to create an image depicting the size or silhouette of different tubers. Chapter 4 discusses effective inversion as an alternate option to gain more information on the tubers. Although effective inversion will not result in exact placement, numbers or size at this stage it is able to approximate the inhomogeneous model and show growth. This growth is shown as the effective diffusion D, which gradually moves towards D_t as tubers grow larger. From the effective diffusion D the relation between soil and tubers may be reverse engineered, which means the total size of the tubers may be found from this constant. In a simple model, as simulated in this report, there are enough assumptions to potentially reconstruct both the number of tubers and their size based the data generated over a whole season. Realistically however, the total amount of tubers has to be calculated in real time and at best based on a previously found D_{eff} in a setting with different tubers growing at different speeds, meaning the number of tubers and their sizes can't be determined uniquely anymore. Effective inversion comes with more restrictions. In the early phases of the growth period the correlation-based functional will not give accurate results, although later results can be extrapolated to correct for this behavior. This also means effective inversion will struggle if there aren't enough tubers or large enough tubers to be measures, as the results over the complete period will be similar to those of the first period of a model with a large enough quantity of tubers.
All simulations done have been in 2D. Simulations in 3D should theoretically give similar results, however, several problems arise. One of these potential problem is the time it will take to obtain D_{eff}. To find D_{eff} multiple simulations will have to be made before a minimum of the cost-functional with respect to D can be decided. In 2D, since the model used in effective inversion is stationary and mostly homogeneous, the time it takes to find D_{eff} will not result in any issues. When expanding to 3D the time it takes will increase exponentially, so the process will need to be optimized.
Furthermore, most simulations are made using a simplified model for the tubers and the trench. As they do not account for tubers growing at different speeds and different times, they also do not account for weather changes. The temperature in the simulations is periodic and follows the same function during the entire period. If temperature changes between day and night are smaller, the average temperature changes during the season or other events like rain occur, it is not yet clear what the result will be. The approximation might be more difficult and results more ambiguous. This will require further investigation to determine.
These limitations need to be considered when assessing the feasibility of subsurface imaging using diurnal temperature variations. The method assessed in this report cannot create an image or silhouette

of the tubers. Thus, individual growth nor the quantity of tubers can be assessed using this method. However, it is possible to give an indication of the growth of tubers as a whole, meaning the method can be used for monitoring the overall growth and size. Therefore, this method is feasible when it comes to monitoring the growth of tubers underground, albeit in less detail than originally expected.

6

Conclusion

In this report the growth of tubers during the entire bulking process has been modelled. The growth process is imitated by creating a trenchlike interface in which circular subdomains are set to grow at equal speeds. The model is numerically approximated using a finite element method and the simulations are subsequently analyzed. The simulations resulted in information regarding temperature changes under the ground as well as the effect on the amplitude and phase shift of these temperature variations. These temperature variations are insufficient regarding visualizing the size or location of the tubers, therefore effective inversion was introduced. A secondary simplified model is simulated and used to approximate the model with tuber by varying the diffusion constant. The value for the diffusion constant that fits the model best is considered the effective diffusion and used to deduce more information from the model. The effective diffusion shows a changing balance between tubers and soil and therefore says something about the number of tubers that are under the ground.
Using these simulations it is demontrated that subsurface imaging using diurnal temperature variations is a feasible solution. The method is likely able to provide an estimation of the total amount of tubers when using a grid of temperature meters placed below the trench, however the model is unable to determine the amount or size of the individual tubers due to being

- ill-posed if the exact number and size of the tubers have to be determined due to the existence of multiple feasible solutions,
- unable to determine the exact location of the tubers and, combined with the above, therefor unable to reconstruct an image of the tubers.

In conclusion, the research presented here shows both the limitations and possibilities of subsurface imaging using diurnal temperature variations. The model simulated for this research still has a several restrictions and limitations, however all the simulations performed here have proven that this method can be used for quantitative analysis of an estimate of the amount of tubers in a testing area. This research has also proven that using the diurnal temperature variations and the differences between the diffusion constants of soil and tubers alone is not enough to fully monitor tuber growth as it is not able to differentiate between individual tubers. The effective diffusion still has to be used to find a ratio between soil and tubers, and therefore determining the number of tubers, and the limitations of this inversion have to be further investigated. Future models can also be made 3D and can be further expanded by

- including tubers that grow at various rates and up to various sizes,
- including varying diurnal temperature changes during the growth period, such as a slowly climbing average temperature or smaller diurnal variations,
- including weather variations, such as rain and a different composition of soil as the soil gets saturated with water.

Bibliography

[1] HZPC. (n.d.). HZPC. Retrieved December , 2019, from
https://www.hzpc.com/

[2] He, X., Lin, T., Lin, Y. & Zhang, X. (2012) Immersed Finite Element methods for Parabolic Equations with Moving Interface, *Wiley Online Library*, DOI: 10.1002/num.21722

[3] Ghosh, S. & Kikuchi, N. (1991) An Arbitrary Lagrangian-Eularian Finite Element Method for Large Deformation Analysis of Elastic-Viscoplasic Solids. *Computer Methods in Applied Mechanics and Engineering, 86,* 127-188

[4] Fenicsproject. (2019). The FEniCS Project 2019.1.0. Retrieved September 2019, from
https://fenicsproject.org/

[5] ICIPE20. (2019). International Conference on Inverse Problems in Engineering. Retrieved December, 2019, from
http://icipe20.univaq.it/wordpress/

[6] Parker, D.F. (2003) *Fields, Flows and Waves, An Introduction to Continuum Models*. London, United Kingdom, Springer.

[7] Budko, N. (2019). *NA08-10 Finite Element Method Part 1-3*. Retrieved from
https://sites.google.com/view/natudelft

[8] van Kan, J., Segal, A. & Vermolen, F.(2014) *Numerical Methods in Scientific Computing*. Delft, the Netherlands, Delft Academic Press.

[9] Jamil, B. & Ahmad, N. (2013) Thermal Diffusivity Variations of Potato During Precooling in Natural Convection Environment. *International Journal of Agriculture and Food Science Technology, 4(3),* 233-238.

[10] Magee, T.R.A & Bransburg, T. (1995) Measurement of Thermal Diffusivity of Potato, Malt Bread and Wheat Flour. *Journal of Food Engineering, 25,* 223-232.

[11] de Jong van Lier, Q. & Durigon, A. (2013) Soil Thermal Diffusivity Estimated from Data of Soil Temperature and Single Soil Component Properties. *Revista Brasileira de Ciência do Solo, 37,* 106-112

[12] Mimouni, T., Lei, L., Laloui, L. (2015) Estimating soil thermal diffusivity with interference analyses. *Acta Geotechnica, 10,* 197-208, DOI: 10.1007/s11440-014-0325-0

[13] Stefan-Boltzmann constant. (2019). In *Wikipedia* Retrieved September 2019 from https://en.wikipedia.org/wiki/Stefan%E2%80%93Boltzmann_constant

[14] Choy, T.C. (1999) *Effective Medium Theory Principles and Application*. Oxford, United Kingdom, Clarendon Press.

[15] Raghunathan, S.B.& Budko, N.V. (2010) Effective permittivity of finite inhomoheneous objects. *Physical review B, 81*, DOI: 10.1103/PhysRevB.81.054206

[16] Budko, N.V. & Remis R.F. (2004) Electromagnetic inversion using a reduced-order three-dimensional homogeneous model *Inverse problems, 20,* DOI: 10.1088/0266-5611/20/6/S02